

1 **Saturation hysteresis effects on the seismic signatures**  
2 **of partially saturated heterogeneous porous rocks**

3 **Santiago G. Solazzi<sup>1,2</sup>, Luis Guarracino<sup>2</sup>, J. Germán Rubino<sup>3</sup>, and Klaus**  
4 **Holliger<sup>1,4</sup>**

5 <sup>1</sup>Applied and Environmental Geophysics Group, Institute of Earth Sciences, University of Lausanne,  
6 Lausanne, Switzerland.

7 <sup>2</sup>CONICET, Facultad de Ciencias Astronómicas y Geofísicas, Universidad Nacional de La Plata, La  
8 Plata, Argentina.

9 <sup>3</sup>CONICET, Centro Atómico Bariloche - CNEA, San Carlos de Bariloche, Argentina.

10 <sup>4</sup>School of Earth Sciences, Zhejiang University, Hangzhou, China.

11 **Key Points:**

- 12 • We present a novel model that allows to include the effects of saturation hystere-  
13 sis on seismic attenuation and phase velocity dispersion.
- 14 • We reproduce key features of the saturation fields and of the seismic signatures  
15 observed during drainage and imbibition experiments.
- 16 • Results show that the pore-scale characteristics can greatly influence the hystere-  
17 sis effects on the seismic signatures.

Published (2019) American Geophysical Union. Further reproduction or electronic distribution is not permitted. Not subject to U.S. copyright. The AGU published article can be found in: <https://doi.org/10.1029/2019JB017726>

---

Corresponding author: Santiago G. Solazzi, [Santiago.Solazzi@unil.ch](mailto:Santiago.Solazzi@unil.ch)

**Abstract**

Experimental evidence indicates that the spatial distribution of immiscible pore fluids in partially saturated media depends on the flow history and, thus, exhibits hysteresis effects. To date, most works concerned with modelling the effective seismic properties of partially saturated rocks either disregard these effects or account for them employing oversimplified approaches. This, in turn, can lead to erroneous interpretations of the corresponding seismic signatures. In this work, we present a novel methodology that allows to compute hysteresis effects on seismic attenuation and dispersion due to mesoscopic wave-induced fluid flow (WIFF) in realistic scenarios. For this purpose, we first employ a constitutive model that considers a porous medium locally as a bundle of constrictive capillary tubes with a fractal pore-size distribution, which allows to estimate local hydraulic properties and capillary pressure-saturation hysteretic relationships in a heterogeneous rock sample. Then, we use a numerical upscaling procedure based on Biot's poroelasticity theory to compute seismic attenuation and velocity dispersion curves during drainage and imbibition cycles. By combining these procedures, we are able to model, for the first time, key features of the saturation field and of the seismic signatures commonly observed in the laboratory during drainage and imbibition experiments. Our results also show that the pore-scale characteristics of a given porous medium, such as the pore-throat geometry, can greatly influence the hysteresis effects on the seismic signatures.

**1 Introduction**

Partially saturated environments are of preeminent importance in many scientific and applied scenarios, such as, groundwater management and remediation, exploration and production of hydrocarbons, and CO<sub>2</sub> geosequestration. Partially saturated geological formations are commonly modelled as porous media whose pore space is occupied simultaneously by two immiscible and mobile fluid phases (e.g., Bear, 1972). These fluid phases are referred to as *wetting* and *non-wetting* in relation to their capacity to wet the pore walls. Interestingly, the spatial distribution of the pore fluids throughout a porous medium is determined by the heterogeneities of the rock frame, the properties of the pore fluids, and by the flow history (e.g., Shi et al., 2011; Alemu et al., 2013). In this context, a fundamental aspect to account for is the irreversibility of multiphase flow dynamics, that is, the *hysteresis* of this physical process.

50 At the microscopic scale, hysteresis is mainly considered to be caused by contact  
51 angle effects (Juanes et al., 2006) and by irregularities in the cross-sections of the pores  
52 that act as “capillary barriers” to the flow of the non-wetting phase (e.g., Lenormand,  
53 1990; Soldi et al., 2017). Hysteretic effects are usually defined in terms of the two ex-  
54 treme cases of immiscible displacement, namely, *imbibition* and *drainage*. Imbibition is  
55 a process where an invading wetting fluid phase displaces an already present non-wetting  
56 phase from the rock pores. Drainage is the inverse process, that is, a non-wetting phase  
57 displaces a wetting phase from the pore space. Employing computer-assisted tomogra-  
58 phy (CT) scans, several experimental works show that drainage and imbibition processes  
59 generate fundamentally different saturation patterns for the same overall saturation state  
60 (e.g., Cadoret et al., 1998; Shi et al., 2011; Alemu et al., 2013). Therefore, hysteretic ef-  
61 fects should be accounted for when trying to characterize the properties of partially sat-  
62 urated media through non-invasive geophysical methods.

63 The seismic method is arguably one of the most employed techniques to explore  
64 the subsurface (e.g., Kearey et al., 2013). Improving the current understanding of the  
65 properties of seismic waves traveling through partially saturated environments could al-  
66 low to extract crucial information, such as permeability field and fluid distribution, from  
67 seismic data. One of the first experimental studies focusing on the impact of saturation  
68 hysteresis on seismic signatures was performed by Knight and Nolen-Hoeksema (1990).  
69 They observed that the relationship between seismic velocity and overall saturation dif-  
70 fers when the saturation state of the probed rock sample is obtained through drainage  
71 or imbibition. Later, Yin et al. (1992) observed a similar behavior on attenuation curves  
72 and attributed their results to wave-induced fluid flow (WIFF) (e.g., Müller et al., 2010)  
73 taking place in the mesoscopic scale range, that is, at scales much larger than the pore  
74 scale but much smaller than the predominant seismic wavelength, between fully water-  
75 saturated regions and their partially saturated surroundings. A common feature of these  
76 experimental studies is that attenuation and phase velocity dispersion values are more  
77 pronounced during drainage than during imbibition. The works of Cadoret et al. (1995,  
78 1998), which explored the behavior of seismic signatures for different frequencies and sat-  
79 urations in partially saturated limestones, shed some light on this particular subject. These  
80 authors employed CT scans to determine the air and water distribution associated with  
81 drainage and imbibition processes. They observed that drainage processes tend to gen-  
82 erate non-uniform fluid distributions characterized by well-defined gas and water patches.

83 Conversely, imbibition processes tend to produce more uniform fluid distributions with  
84 smoother transitions between the water-saturated patches and their surroundings. The  
85 more accentuated mechanical compressibility contrasts generated by drainage would there-  
86 fore be expected to produce higher dissipation due to WIFF than those resulting from  
87 imbibition experiments. It is worth mentioning that not all the works studying the ef-  
88 fects of hysteresis on the seismic signatures of porous rocks evidence such behavior (e.g.,  
89 Nakagawa et al., 2013; Alemu et al., 2013; Zhang et al., 2015). Hence, the complexity  
90 of hysteresis processes should be further analyzed if we wish to discern the physical mech-  
91 anisms that control the characteristics of the saturation distribution and of the associ-  
92 ated seismic response.

93 To date, theoretical works accounting for hysteretic effects on the seismic signa-  
94 tures of partially saturated media rely on simplifying assumptions that limit a rigorous  
95 interpretation of the governing physical processes. Akbar et al. (1994) and Papageorgiou  
96 and Chapman (2015) modelled saturation hysteresis effects on squirt flow. Although the  
97 squirt flow models proposed by these works are fundamentally different, they both con-  
98 sider that the porous medium is composed by stiff pores and compliant “cracks” and use  
99 simple models to saturate these regions. Le Ravalec et al. (1996) proposed a model to  
100 account for the effects of hysteresis on seismic phase velocities due to mesoscopic WIFF  
101 and squirt flow. These authors consider partially saturated spherical patches to model  
102 mesoscopic WIFF effects and round pore and spheroidal crack geometries to model squirt  
103 flow effects. In this model, local saturation depends on the drainage or imbibition pro-  
104 cesses. It is important to remark here that all the above mentioned models assume that  
105 the rock samples are homogeneous with regard to porosity and permeability. However,  
106 experimental evidence shows that even clean and well-sorted sandstone samples tend to  
107 exhibit substantial fluctuations of their hydraulic properties (e.g., Krause et al., 2013;  
108 Li & Benson, 2015). Without the existence of such heterogeneities to trap the pore flu-  
109 ids, mesoscopic scale fluid patches would migrate due to buoyant forces and diffuse due  
110 to the effects of capillary pressure gradients (e.g., Krevor et al., 2011). In this sense, lab-  
111 oratory measurements show conclusively that the fluid distribution is conditioned by the  
112 rock frame hydraulic properties (e.g., Shi et al., 2011; Alemu et al., 2013). In such con-  
113 text, Ba et al. (2015) proposed a double-porosity model, considering spherical patches  
114 and heterogeneous samples, in which hysteretic effects are included by assuming differ-  
115 ent saturation or desaturation scenarios. However, the considered fluid patches are not

116 directly associated with changes in the hydraulic properties of the rock frame. Further-  
117 more, the spherical patch geometry employed by Ba et al. (2015) and Le Ravalec et al.  
118 (1996) imposes an unrealistically sharp transition of physical properties between the meso-  
119 scopic patches and their surroundings, which has a strong impact on the seismic signa-  
120 tures (Rubino & Holliger, 2012; Solazzi, 2018). Notably, the available evidence from lab-  
121 oratory experiments points to spatially continuous variations of the fluid distributions  
122 in partially saturated porous media (e.g., Toms-Stewart et al., 2009; Shi et al., 2011).  
123 To our knowledge, saturation hysteresis effects on mesoscopic WIFF have so far not been  
124 studied considering realistic spatially continuous saturation patterns governed by vari-  
125 ations of the rock frame properties.

126 In this work, we present a novel model that allows to include the effects of satu-  
127 ration hysteresis on seismic attenuation and phase velocity dispersion due to mesoscopic  
128 WIFF in heterogeneous porous media. For this purpose, we employ a pore-scale model  
129 which considers the porous medium as a bundle of constrictive capillary tubes with a  
130 fractal pore size distribution (Soldi et al., 2017). This physically-based model has the  
131 advantage of providing closed analytical expressions for the porosity, the permeability,  
132 and the primary drainage and imbibition capillary pressure-saturation curves for a ho-  
133 mogeneous porous medium. By assuming that the different regions of a heterogeneous  
134 rock sample are locally described by this constitutive model and considering a set of cap-  
135 illary equilibrium states, we obtain pore fluid distributions representative of both drainage  
136 and imbibition cycles. We then apply a numerical upscaling procedure based on Biot's  
137 theory of poroelasticity to compute seismic attenuation and dispersion curves due to WIFF  
138 produced by the heterogeneous fluid distribution. We explore the impact of saturation  
139 hysteresis on the fluid distribution and on the seismic signatures for different overall sat-  
140 urations and frequencies. Finally, we analyze the effects of the pore geometry on the hys-  
141 teresis phenomenon. The proposed model permits to reproduce key features of the fluid  
142 distribution and of the seismic signatures observed in the laboratory during drainage and  
143 imbibition processes and, thus, allows for a better understanding of the WIFF phenomenon  
144 in partially saturated environments.

## 145 **2 Theoretical Background and Numerical Models**

146 In this section, we introduce the constitutive model of Soldi et al. (2017), which  
147 allows to obtain the porosity, the permeability, and the hysteretic capillary pressure-saturation

148 curves of a porous medium characterized by a given pore space topology. Subsequently,  
149 we employ these relationships to determine the local hydraulic properties of a hetero-  
150 geneous synthetic rock sample and, in particular, to generate saturation fields represen-  
151 tative of drainage and imbibition processes. Finally, we present an upscaling procedure  
152 (Rubino et al., 2009) based on Biot’s poroelasticity theory (Biot, 1941) to estimate the  
153 seismic attenuation and phase velocity dispersion of the numerical rock sample account-  
154 ing for hysteresis effects.

## 155 **2.1 Hysteretic Model for Partially Saturated Rocks**

156 Capillary forces play a predominant role in the flow of immiscible fluid phases through  
157 porous formations. Interestingly, the distribution of immiscible fluid phases during capillary-  
158 driven flow is determined by mechanisms that take place at the pore scale (e.g., Lenor-  
159 mand et al., 1983). In this sense, microscopic processes provide the foundations for un-  
160 derstanding and predicting two-phase flow at the field scale (e.g., Juanes et al., 2006).

161 At the macroscopic scale, the hysteresis process manifests itself through the depen-  
162 dence of the relative permeabilities and capillary pressures on the saturation history. Note  
163 that constitutive relationships, such as those of Brooks and Corey (1964) or van Genuchten  
164 (1980), have to be adapted to be history-dependent to account for this characteristic (e.g.,  
165 Hogarth et al., 1988; Lenhard et al., 1991). Particularly, constitutive models based on  
166 capillary tubes have been proven to be useful to characterize porous media when describ-  
167 ing hydrological processes and hydraulic properties for different granulometries (e.g., Tyler  
168 & Wheatcraft, 1990; Yu et al., 2003; Guarracino et al., 2014; Xu, 2015). These models  
169 derive the hydraulic properties of a given porous medium considering that, in the pres-  
170 ence of a fluid pressure gradient, flow channels are generated within the pore space. The  
171 characteristics of these channels are then modelled employing the capillary tube geom-  
172 etry considering different shapes and aperture distributions. If the rock is isotropic, the  
173 derived hydraulic properties are independent of the flow direction. In this context, Soldi  
174 et al. (2017) proposed a hysteretic constitutive model for partially saturated flow assum-  
175 ing that porous media can be conceptualized as a bundle of constrictive capillary tubes  
176 with a fractal distribution of the radii. Individual pores are modelled as cylindrical tubes  
177 of radius  $r$  connected by periodical throats (Figure 1). Based on physical and geomet-  
178 rical concepts, closed-form equations for the porosity and permeability can be obtained  
179 by volume integration. Also, the chosen conceptualization of the pore geometry allows

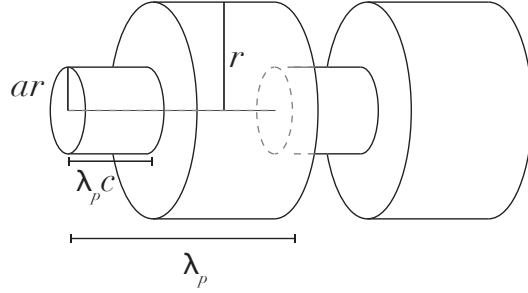


**Figure 1.** Pore geometry of a capillary tube of radius  $r$ .  $\lambda_p$  is the period of the pore structure. The throats have radii and lengths given by  $a \cdot r$  and  $\lambda_p \cdot c$ , respectively.

180 to model hysteresis due to “capillary barrier” effects in the capillary pressure-saturation  
 181 functions. In this work, we use the model proposed by Soldi et al. (2017), whose char-  
 182 acteristics are outlined below, to develop realistic partially saturated environments ac-  
 183 counting for hysteresis effects.

184 Let us consider a representative elementary volume (REV) of a porous medium whose  
 185 pore structure is represented by a bundle of constrictive tubes with varying radii  $r$ . Each  
 186 constrictive tube is characterized by a spatial period  $\lambda_p$ , a radial factor  $0 < a \leq 1$ ,  
 187 and a length factor  $0 \leq c \leq 1$  (Figure 1). The radial factor  $a$  represents the throat-  
 188 to-pore size ratio and the length factor  $c$  represents the fraction of  $\lambda_p$  with a narrow throat.  
 189 The cumulative size distribution of the pores obeys a fractal law (e.g., Guarracino, 2007;  
 190 Yu et al., 2003)

$$191 \quad N(r) = \left(\frac{r}{R}\right)^{-D}, \quad r_{min} \leq r \leq r_{max}, \quad (1)$$

192 where  $R$  is the characteristic size of the REV,  $1 < D < 2$  is the fractal dimension, and  
 193  $r_{min}$  and  $r_{max}$  are the minimum and maximum pore radii, respectively.

194 By means of volume integration, it is found that the porosity  $\phi$  of the REV is given  
 195 by (Soldi et al., 2017)

$$196 \quad \phi = \frac{f_v D}{R^{(2-D)}(2-D)} \left[ r_{max}^{(2-D)} - r_{min}^{(2-D)} \right], \quad (2)$$

197 where  $f_v = a^2 c + 1 - c$ . The factor  $f_v$  varies between 0 and 1 and quantifies the poros-  
 198 ity reduction due to the constrictivity of pores. Also, by integrating the flow rate and

199 employing Darcy's law, Soldi et al. (2017) inferred the effective permeability  $\kappa$  as

$$200 \quad \kappa = \frac{f_k D}{8R^{(2-D)}(4-D)} \left[ r_{max}^{(4-D)} - r_{min}^{(4-D)} \right], \quad (3)$$

201 where  $f_k = a^4 / [c + a^4(1 - c)]$ . The factor  $f_k$  also varies between 0 and 1 and quan-  
202 tifies the permeability reduction due to the pore constrictivity.

203 As previously stated, the pore-scale geometry illustrated in Figure 1 permits to in-  
204 clude hysteresis effects associated with the capillary pressure-saturation curve. Recall  
205 that, for a straight tube of radius  $r_p$ , the capillary pressure  $p_c$  can be expressed as (Bear,  
206 1972)

$$207 \quad p_c = \frac{2\gamma \cos(\beta)}{r_p}, \quad (4)$$

208 where  $\gamma$  is the interfacial tension between the two immiscible phases that occupy the pore  
209 space and  $\beta$  the contact angle of the corresponding interface with the pore wall. Due to  
210 the varying aperture of the pores, drainage and imbibition processes exhibit distinct be-  
211 haviors. In an imbibition process, capillary pressure drops as the porous rock is invaded  
212 by the wetting fluid. Following equation (4), smaller pores are wetted in the early stages  
213 of the process and larger pores follow. During a drainage process, capillary pressure in-  
214 creases as the pores are invaded by the non-wetting fluid. However, the process is con-  
215 ditioned by the throat size that connects the pores. Consequently, pores connected by  
216 thick throats are drained first and pores connected by narrow throats follow.

217 The main drainage capillary pressure-saturation curve is obtained by assuming that  
218 a pore becomes fully saturated by the non-wetting fluid if the radius of the pore throat  
219  $r_{th} = ar$  is greater than the radius  $r_p$  given by equation (4). Then, it is reasonable to  
220 conclude that pores with radii  $r$  between  $r_{min}$  and  $r_p/a$  remain fully saturated by the  
221 wetting fluid. The closed-form analytical expression that relates the effective wetting fluid  
222 saturation and the capillary pressure for the drainage cycle  $S_{ew}^d(p_c)$  is (Soldi et al., 2017)

$$223 \quad S_{ew}^d(p_c) = \begin{cases} 1, & \text{if } p_c \leq \frac{p_{c,min}}{a}, \\ \frac{(p_c a)^{(D-2)} - p_{c,max}^{(D-2)}}{p_{c,min}^{(D-2)} - p_{c,max}^{(D-2)}}, & \text{if } \frac{p_{c,min}}{a} \leq p_c \leq \frac{p_{c,max}}{a}, \\ 0, & \text{if } p_c \geq \frac{p_{c,max}}{a}, \end{cases} \quad (5)$$

224 where  $p_{c,min} = 2\gamma \cos(\beta)/r_{max}$  and  $p_{c,max} = 2\gamma \cos(\beta)/r_{min}$  are the minimum and  
225 maximum capillary pressures, respectively.

226 Similarly, the main imbibition capillary pressure-saturation curve can be obtained  
227 assuming that only the tubes with radius  $r < r_p$  will be fully saturated by the wetting



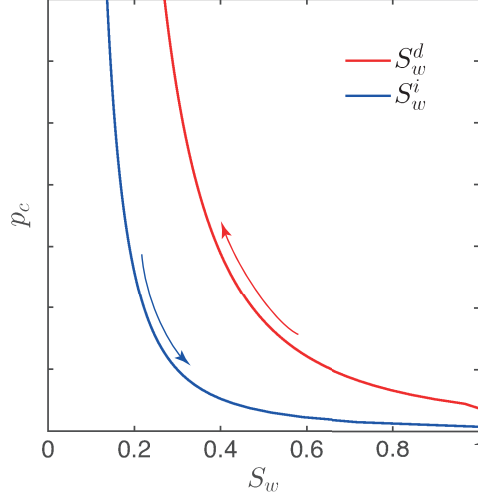


**Figure 2.** General behavior of the capillary pressure curves as a function of wetting phase saturation for drainage (red solid line) and imbibition (blue solid line) resulting from the hysteretic constitutive model.

228 fluid. Then, the effective wetting phase saturation for the main imbibition curve  $S_{ew}^i(p_c)$   
 229 can be expressed as (Soldi et al., 2017)

$$230 \quad S_{ew}^i(p_c) = \begin{cases} 1, & \text{if } p_c \leq p_{c,min}, \\ \frac{p_c^{(D-2)} - p_{c,max}^{(D-2)}}{p_{c,min}^{(D-2)} - p_{c,max}^{(D-2)}}, & \text{if } p_{c,min} \leq p_c \leq p_{c,max}, \\ 0, & \text{if } p_c \geq p_{c,max}. \end{cases} \quad (6)$$

231 The saturation of the wetting phase can be obtained from equations (5) and (6)  
 232 by means of  $S_w^q = S_{ew}^q(1 - S_{wr}) + S_{wr}$  with  $q = i, d$ , where  $S_{wr}$  is the residual wetting  
 233 phase saturation of the REV.

234 Figure 2 illustrates the general behavior of the main drainage (red solid curve) and  
 235 imbibition (blue solid curve) capillary pressure curves as a function of wetting phase sat-  
 236 uration resulting from equations (5) and (6). Due to the hysteretic nature of the pro-  
 237 posed constitutive relationships, drainage and imbibition curves differ. Note that, for a  
 238 given capillary pressure value, drainage curves are associated with higher saturation val-  
 239 ues than imbibition curves. It is important to remark that the hysteretic behavior de-  
 240 scribed by equations (5) and (6) is conditioned by the radial factor  $a$ . That is, for  $a =$   
 241 1 drainage and imbibition capillary pressure-saturation curves are identical.

242 The constitutive model presented in this section has the advantage of providing sim-  
 243 ple analytical expressions for porosity, permeability, and hysteretic capillary pressure-  
 244 saturation functions for a homogeneous porous medium. We shall use these expressions  
 245 to locally characterize a heterogeneous porous medium, assuming that each region of the  
 246 rock sample is described by a particular set of pore geometry parameters ( $r_{max}$ ,  $r_{min}$ ,  
 247  $a$ ,  $c$ ,  $R$ , and  $D$ ). Then, by assuming different stages of capillary pressure equilibrium at  
 248 the sample's scale, we are able to compute heterogeneous saturation patterns which are  
 249 representative of drainage and imbibition processes.

## 250 2.2 Numerical Upscaling Procedure for Quantifying WIFF Effects

251 Whenever a seismic wave propagates through a porous medium that contains meso-  
 252 scopic heterogeneities, local gradients in the pore fluid pressure arise due to the uneven  
 253 response of the different regions of the rock to the stresses associated with the passing  
 254 wavefield (e.g., Pride, 2005). These pressure gradients induce viscous fluid flow and, thus,  
 255 energy dissipation through internal friction. This mechanism, known as mesoscopic WIFF,  
 256 can generate significant attenuation and velocity dispersion within the seismic exploration  
 257 frequency band (Müller et al., 2010). A particularly interesting characteristic of the WIFF  
 258 process is that it is sensitive to the hydraulic properties of the heterogeneous rock and  
 259 to the geometrical characteristics of the pore fluid patterns (Rubino & Holliger, 2012;  
 260 Masson & Pride, 2011). Consequently, hysteretic effects are expected to have a profound  
 261 impact on seismic attenuation and phase velocity dispersion related to this mechanism.

262 In order to quantify WIFF effects produced by 2D heterogeneous partially satu-  
 263 rated rocks, saturated following the procedure described in the previous subsection, we  
 264 apply the numerical upscaling procedure proposed by Rubino et al. (2009). That is, we  
 265 impose a homogeneous time-harmonic vertical solid displacement of the form  $-\Delta u e^{i\omega t}$   
 266 along the top boundary of a bidimensional square representative sample of the explored  
 267 formation, where  $\omega$  is the angular frequency. In addition, no-flow conditions are imposed  
 268 on all four boundaries and no tangential forces are applied. The solid is neither allowed  
 269 to move vertically on the bottom boundary nor to have horizontal displacements on the  
 270 lateral boundaries. The response of the sample subjected to this relaxation test is ob-  
 271 tained by solving Biot's consolidation equations (Biot, 1941) under appropriate bound-  
 272 ary conditions. Under the assumption that the volume-averaged response of the sam-  
 273 ple can be represented with an equivalent homogeneous viscoelastic solid, an equivalent

274 complex-valued frequency-dependent plane wave modulus  $M_c(\omega)$  is obtained. The in-  
 275 verse quality factor and phase velocity can be computed as (e.g., Borchardt, 2009)

$$276 \quad Q_p^{-1}(\omega) = \frac{\Im\{M_c(\omega)\}}{\Re\{M_c(\omega)\}}, \quad (7)$$

$$277 \quad V_p(\omega) = \left[ \Re \left\{ \sqrt{\frac{\langle \rho_b \rangle}{M_c(\omega)}} \right\} \right]^{-1}, \quad (8)$$

279 where  $\langle \rho_b \rangle$  is the volume average of the bulk density of the aggregate and  $\Re$  and  $\Im$  de-  
 280 note the real and imaginary parts, respectively. The local bulk density is given by

$$281 \quad \rho_b = (1 - \phi)\rho_s + \phi\rho_f, \quad (9)$$

282 where  $\rho_s$  and  $\rho_f$  are the densities of the solid grains and the fluid phase, respectively.  
 283 Appendix A provides the details of this numerical upscaling procedure.

284 Please note that Biot's theory is based on the assumption of a single pore fluid phase.  
 285 However, in a partially saturated medium, each cell of the numerical rock sample con-  
 286 sidered in the upscaling procedure may be saturated by both immiscible phases. There-  
 287 fore, we locally employ an effective fluid phase when solving poroelastic equations A1  
 288 to A4. That is, at each computational cell we define an effective single phase fluid with  
 289 properties determined by those of the individual fluid phases and weighted by their sat-  
 290 uration values (Rubino & Holliger, 2012). Then, the density of the effective fluid is given  
 291 by

$$292 \quad \rho_f = S_w\rho_w + (1 - S_w)\rho_n, \quad (10)$$

293 where  $\rho_w$  and  $\rho_n$  are the wetting and non-wetting phase densities, respectively.

294 As previously stated, the compressibility of the effective fluid is a crucial param-  
 295 eter in the WIFF process. Provided that we consider computational cells having sizes  
 296 much smaller than the diffusion lengths associated with the WIFF process, the fluid pres-  
 297 sure perturbations caused by the seismic wavefield have enough time to equilibrate within  
 298 each computational cell. Hence, the fluid pressure within each cell is uniform and we can  
 299 use Wood's law to obtain the bulk modulus of the effective fluid (Wood, 1955; Mavko  
 300 et al., 2009; Rubino & Holliger, 2012)

$$301 \quad \frac{1}{K_f} = \frac{(1 - S_w)}{K_n} + \frac{S_w}{K_w}, \quad (11)$$

302 where  $K_n$  and  $K_w$  are the bulk moduli of the non-wetting and wetting phases, respec-  
 303 tively.

304 On the other hand, we use the relation of Teja and Rice (1981) to obtain the vis-  
 305 cosity of the two-phase pore fluid mixture in each cell

$$306 \quad \eta_f = \eta_n \left( \frac{\eta_w}{\eta_n} \right)^{S_w}, \quad (12)$$

307 where  $\eta_w$  and  $\eta_n$  denote the viscosities of the wetting and non-wetting phases, respec-  
 308 tively.

309 It is important to remark here that, even though we do consider the effects of cap-  
 310 illary forces to determine the pore fluid distribution, capillary pressure is not accounted  
 311 for when quantifying WIFF effects, as a single fluid with effective properties is consid-  
 312 ered in Biot's equations. Please also note that in this study we analyze hysteresis effects  
 313 on WIFF at the mesoscopic scale and, thus, effects associated with fluid pressure diffu-  
 314 sion at the pore scale are not accounted for in our model. Even though squirt flow ef-  
 315 fects are beyond the scope of this work, it is worthwhile to mention that they can indeed  
 316 be modelled in conjunction with mesoscopic WIFF (e.g., Rubino et al., 2013). For this,  
 317 both microscopic and mesoscopic WIFF models should be based on a unique and con-  
 318 sistent pore scale conceptualization.

### 319 **3 Numerical Analysis**

#### 320 **3.1 Heterogeneous Rock Sample and Physical Properties**

321 In the following, we explore the seismic response of a partially saturated porous  
 322 medium during drainage and imbibition cycles. To do so, we analyze the behavior of a  
 323 square 2D synthetic rock sample of 3-m side length with properties representative of a  
 324 heterogeneous Fontainebleau sandstone (e.g., Bourbié & Zinszner, 1985). We assume that  
 325 the sample contains spatially continuous variations of the dry frame properties, which  
 326 are parameterized as functions of the maximum pore radius. In particular, the spatial  
 327 distribution of  $r_{max}$ , shown in Figure 3a, is obtained by means of a stochastic procedure  
 328 based on a von-Karman-type spectral density function (Tronicke & Holliger, 2005). To  
 329 this end we consider a stochastic process with a spatially isotropic correlation length of  
 330 25 cm and a Hurst number of 0.1. The minimum pore radius in each cell of the rock sam-  
 331 ple is considered to obey  $r_{min} = 10^{-1} r_{max}$ . The resulting range of variations of both  
 332  $r_{max}$  and  $r_{min}$  is consistent with experimental measurements performed in Fontainebleau  
 333 sandstones (e.g., Dong & Blunt, 2009).

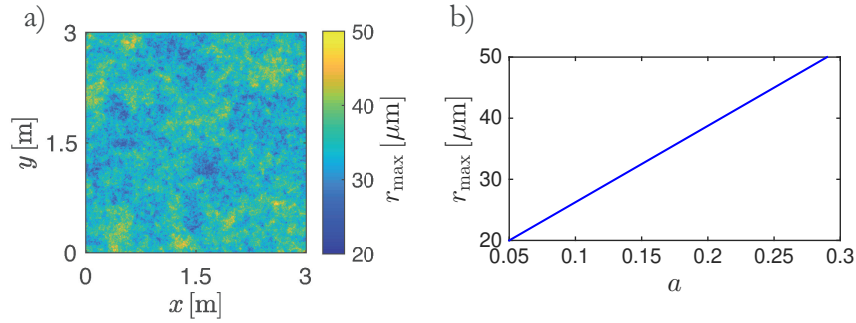


**Figure 3.** (a) 2D heterogeneous distribution of maximum pore radii  $r_{max}$  and (b) relationship between  $r_{max}$  and the radial factor  $a$  considered in the numerical simulations.

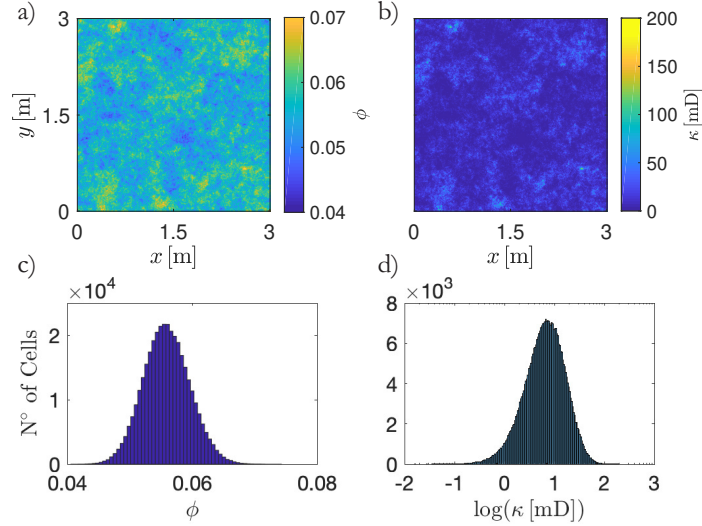
334 Recall that, within each cell of the synthetic rock sample, the pore space is assumed  
 335 to be composed of a fractal distribution of capillary tubes, which, in turn, are charac-  
 336 terized by an alternation between pores with radii  $r_{min} \leq r \leq r_{max}$  and throats with  
 337 radii  $r_{th} = ra$  (Figure 1). The former account for most of the porosity while the lat-  
 338 ter control the flow properties. Doyen (1988) analyzed the pore space characteristics of  
 339 a set of Fontainebleau sandstone samples with different porosities. The corresponding  
 340 measurements show that the characteristic throat-to-pore size ratio, that is, the radial  
 341 factor  $a$ , increases as the average pore-size increases. Furthermore, these measurements  
 342 show a largely linear relationship between  $a$  and the average pore-size. Based on this ex-  
 343 perimental evidence, we assume that  $a$  and  $r_{max}$  are linearly related (Figure 3b). The  
 344 characteristics of this relation will be further discussed in Section 3.4.

345 We consider a fractal dimension  $D = 1.465$  in agreement with the typical values  
 346 for sandy porous media found by Tyler and Wheatcraft (1990). For the sake of simplic-  
 347 ity, we assume this value to be spatially constant. The parameter  $R$  is taken to be the  
 348 cell side length of the computational mesh. Finally, the parameter  $c$  is assumed to be  
 349 spatially constant and is adjusted to obtain porosity and permeability fields whose mean  
 350 values are consistent with measurements performed by Bourbié and Zinszner (1985) on  
 351 Fontainebleau sandstones. The parameters employed to generate the numerical rock sam-  
 352 ple are summarized in Table 1.

353 Once the parameters of the hysteretic model are defined at each cell, equations (2)  
 354 and (3) allow to obtain the local porosity and permeability values. As shown in Figure  
 355 4, the considered rock sample is characterized by heterogeneous porosity (Figure 4a) and

**Table 1.** Mean values for the parameters of the pore-scale model employed to generate the synthetic rock sample.

$\langle r_{max} \rangle$	$\langle a \rangle$	$c$	$D$	$R$
33 [ $\mu\text{m}$ ]	0.16	0.6	1.465	5 [ $\text{mm}$ ]

**Figure 4.** 2D heterogeneous a) porosity and b) permeability fields obtained from the constitutive pore-scale model. Panels c) and d) show the histograms of the corresponding fields.

356 permeability (Figure 4b) fields, whose mean values are  $\langle \phi \rangle = 5.5\%$  and  $\langle \kappa \rangle = 9.35 \text{ mD}$ ,  
 357 respectively. Figures 4c and 4d show the corresponding histograms.

358 The pore fluids employed in the simulations are air and water, whose properties  
 359 are given in Table 2. As both fluids are immiscible, their interfaces within the capillary  
 360 tubes are characterized by a given contact angle  $\beta$  and interfacial tension  $\gamma$ . The con-  
 361 tact angle is taken as  $\beta = 0^\circ$  and the interfacial tension as  $\gamma = 72 \text{ mN/m}$ , in agree-  
 362 ment with the approximate properties of water-air interfaces at a temperature of  $20^\circ \text{ C}$   
 363 and at atmospheric pressure (e.g., Vargaftik et al., 1983). For the sake of simplicity, we  
 364 assume that these parameters remain constant during drainage and imbibition cycles.  
 365 Note that these parameters may experience small changes, whose effects are, however,  
 366 beyond the scope of this work.

**Table 2.** Material properties for the fluids and the solid matrix of the synthetic sandstone sample considered in this study. Adopted from Rubino and Holliger (2012), Rubino et al. (2011) and Tisato and Quintal (2013)

Solid phase			
Quartz	$K_s = 37 \text{ GPa}$	$\mu_s = 44 \text{ GPa}$	$\rho_s = 2.64 \text{ g/cm}^3$
Fluid phases			
Water	$K_w = 2.3 \text{ GPa}$	$\eta_w = 0.001 \text{ Pa s}$	$\rho_w = 1.0 \text{ g/cm}^3$
Air	$K_n = 1 \times 10^{-4} \text{ GPa}$	$\eta_n = 2 \times 10^{-5} \text{ Pa s}$	$\rho_n = 0.001 \text{ g/cm}^3$

The residual saturation  $S_{wr}$  at each computational cell of the rock sample is computed following Timur's empirical equation (e.g., Timur, 1968; Mavko et al., 2009)

$$S_{w,r} = \sqrt{\frac{8.58 \phi^{4.4}}{\kappa}}, \quad (13)$$

with the permeability  $\kappa$  in units of Darcy [D].

Finally, the bulk and shear moduli of the dry matrix are computed at each cell using Pride's model (Pride, 2005)

$$K_m = K_s \frac{(1 - \phi)}{(1 + c_s \phi)}, \quad (14)$$

$$\mu_m = \mu_s \frac{(1 - \phi)}{(1 + 1.5c_s \phi)}, \quad (15)$$

where  $K_s$  and  $\mu_s$  denote the bulk and shear moduli of the solid grains, respectively. The values for these parameters are given in Table 2. The degree of cohesion between the grains is given by the so-called consolidation parameter  $c_s$ , which ranges from 2 to 20 (Pride, 2005). We use a value of  $c_s = 13$ , which, according to equations (14) and (15), is consistent with the dry frame properties of low-porosity Fontainebleau sandstones (Subramaniyan et al., 2015).

Note that each cell of the numerical rock sample is characterized by a particular pair of drainage and imbibition capillary pressure-saturation curves. Hence, by assuming a constant capillary pressure state for the whole sample, one can obtain the saturation at each cell using equations (4), (5), and (6).

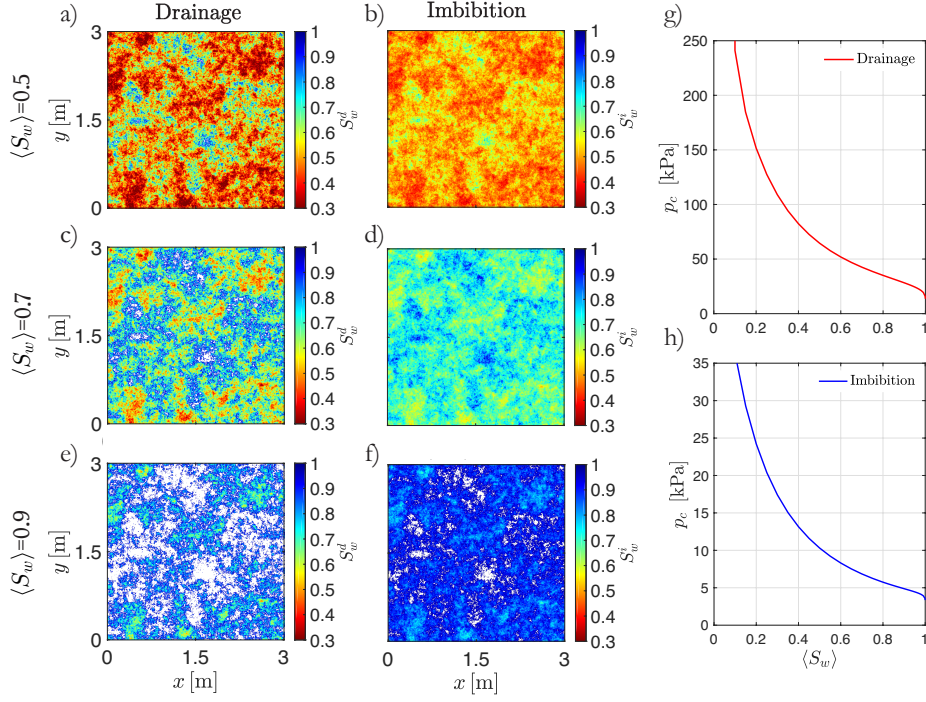


**Figure 5.** Saturation fields obtained through the proposed model following a drainage (left column) or an imbibition (central column) cycle for the following overall saturations levels: (a) and (b)  $\langle S_w \rangle = 0.5$ ; (c) and (d)  $\langle S_w \rangle = 0.7$ ; and (e) and (f)  $\langle S_w \rangle = 0.9$ . White regions represent the zones where  $K_f \geq 0.5K_w$ . Panels (g) and (h) illustrate the capillary pressure-saturation relationships for drainage and imbibition, respectively.

386

### 3.2 Hysteretic Saturation Patterns

387

388

389

Figure 5 shows hysteretic saturation fields associated with drainage and imbibition cycles following the procedure described above. We illustrate these fields at different overall saturation values, which respond to

390

$$\langle S_w \rangle = \frac{\sum_{ij} S_w(\Omega_{ij}) \phi(\Omega_{ij})}{\sum_{ij} \phi(\Omega_{ij})}, \quad (16)$$

391

392

393

394

395

where  $\Omega_{ij}$  denotes the  $ij$ th cell of the employed square computational mesh. The left column of Figure 5 illustrates the evolution of the saturation fields associated with the drainage cycle and the central column illustrates the corresponding evolution associated with the imbibition cycle. The right column shows the capillary pressure-saturation relationships for drainage (red line) and imbibition (blue line) associated with the probed sample.

396

397

Figures 5a, 5c, and 5e show that during a drainage experiment the saturation field tends to present regions mainly saturated by water surrounded by zones partially sat-



398 urated with air and water. To allow for a better interpretation of these fields, the regions  
399 where water saturation is  $S_w > 0.9999$  are colored with white. These regions, from now  
400 on, will be referred to as *water patches* and correspond to the zones where the bulk mod-  
401 ulus of the effective pore fluid fulfills  $K_f \geq 1/2K_w$ . That is, these are the regions that  
402 behave from a mechanical point of view as water-saturated. The remaining regions of  
403 the sample behave effectively as air-saturated. By comparison of these fields with Fig-  
404 ure 4, we observe that the regions containing relatively high amounts of air are associ-  
405 ated with high porosity and high permeability zones. This is expected, as the non-wetting  
406 phase percolates first into the regions where throat radii are bigger and capillary resis-  
407 tance is comparatively low. As a counterpart of this behavior, the wetting phase remains  
408 in the zones characterized by small throat radii. Several experimental works have ob-  
409 served this correlation between the non-wetting phase saturation and the zones of high  
410 porosity and permeability in heterogeneous partially saturated porous rocks (Perrin &  
411 Benson, 2010; Shi et al., 2011; Pini et al., 2012; Alemu et al., 2013; Zhang et al., 2015)

412 During an imbibition process (Figures 5b, 5d, and 5f), we observe fluid distribu-  
413 tions which are different from those obtained during drainage, thus evidencing the ef-  
414 fects of saturation hysteresis. By performing a row-by-row comparison between the mod-  
415 elled imbibition and drainage saturation fields, we note that the water patches tend to  
416 appear at lower overall saturations during drainage than during imbibition. Also, we ob-  
417 serve that during imbibition water patches have a smaller characteristic size than those  
418 associated with drainage for the same overall saturation. More importantly, the tran-  
419 sitions between the water patches and their surroundings during imbibition are broad,  
420 partially saturated regions with smoothly varying values. However, during drainage, the  
421 spatial variation of local saturation between water patches and their surroundings is more  
422 abrupt. This characteristic of saturation hysteresis has also been observed through CT  
423 scans in the laboratory when comparing the saturation fields resulting from drainage and  
424 imbibition processes (e.g., Cadoret et al., 1998).

425 Figures 5g and 5h show the capillary pressure-overall saturation relationships for  
426 the probed sample during drainage and imbibition, respectively. We observe that the cap-  
427 illary pressure values during drainage are higher than those arising during imbibition for  
428 the same overall saturation value, thus exhibiting hysteresis effects. The differences in  
429 the spatial pore fluid distributions between drainage and imbibition processes are expected

430 to affect the seismic attenuation and velocity dispersion characteristics due to WIFF at  
 431 the mesoscopic scale.

### 432 **3.3 Seismic Attenuation and Phase Velocity Dispersion**

433 The effects of saturation hysteresis on seismic signatures are explored by subject-  
 434 ing the synthetic rock sample, saturated by the previously generated hysteretic fields,  
 435 to the numerical oscillatory relaxation experiment described in Section 2.2. As a result,  
 436 we obtain the frequency dependent P-wave attenuation and phase velocity at different  
 437 stages of saturation representative of drainage and imbibition experiments. It is impor-  
 438 tant to remark here that as porosity and permeability fields vary smoothly in space they  
 439 do not generate WIFF *per se* at a state of full saturation. Thus, the seismic attenuation  
 440 and velocity dispersion curves analyzed in the following arise due to the presence of het-  
 441 erogeneities in the distribution of the pore fluids.

442 Arguably, one of the most studied characteristics of seismic attenuation and phase  
 443 velocity dispersion is their dependence on the overall saturation (e.g., Gassmann, 1951;  
 444 Lebedev et al., 2009; Monsen & Johnstad, 2005). Figure 6 shows the phase velocity and  
 445 the inverse quality factor as a function of overall saturation for drainage (red lines) and  
 446 imbibition (blue lines) cycles. The seismic response is illustrated considering two frequen-  
 447 cies: 30 Hz (solid lines) and 2 kHz (dashed lines). These frequencies lie within the seis-  
 448 mic and sonic frequency bands, respectively, which are commonly employed in field and  
 449 laboratory experiments (e.g., Tisato & Quintal, 2013; Chapman et al., 2016; Cadoret et  
 450 al., 1995; Bourbié & Zinszner, 1985; Yin et al., 1992). To allow for a better interpreta-  
 451 tion of the velocity curves, we plot in Figure 6a the Gassmann-Wood (GW) and Gassmann-  
 452 Hill (GH) models, that is, the lower and upper limits of the phase velocity, respectively  
 453 (e.g., Mavko et al., 2009). These two models permit a direct evaluation of the level of  
 454 dispersion associated with each curve. It is important to recall that the GW and GH mod-  
 455 els are defined for homogeneous media. As the probed sample is heterogeneous, we have  
 456 employed equivalent effective properties for  $K_m$ ,  $\mu_m$ , and  $\rho_b$  to approximate the behav-  
 457 ior of these curves. Further details regarding the calculation of the GW and GH curves  
 458 considering equivalent effective properties are given in Appendix B.

459 In Figure 6a we observe that, for relatively low overall water saturations,  $V_p$  val-  
 460 ues drop slightly or are fairly stable as the overall saturation of the sample increases. In

461 this context, the average bulk density of the sample increases and its effect is compara-  
 462 ble or greater than that of the plane wave modulus (see equation (8)). However, when  
 463 the porous medium approaches full water saturation, the plane wave modulus increases  
 464 drastically, thus dominating the behavior of the phase velocity. It is important to no-  
 465 tice that, for a given overall saturation state, velocities increase with frequency due to  
 466 WIFF effects. We also observe that phase velocities during drainage depart from the GW  
 467 limit at lower overall saturation values than those associated with imbibition. For ex-  
 468 ample, considering a relative measurement accuracy of 1% for the phase velocity (Bourbié  
 469 & Zinszner, 1985), the dispersion values expressed in Figure 6a for a frequency of 2 kHz  
 470 are experimentally measurable for saturations above 0.86 for drainage and above 0.93  
 471 for imbibition. We also observe that the phase velocity values are higher during drainage  
 472 than during imbibition irrespective of the frequency. A similar behavior has been observed  
 473 experimentally in partially saturated rock samples by Knight and Nolen-Hoeksema (1990)  
 474 and Cadoret et al. (1995). In this sense, our results show that saturation hysteresis due  
 475 to the “capillary barrier” effect constitutes a physical explanation for the characteris-  
 476 tics of the phase velocity-saturation relation during drainage and imbibition observed  
 477 in these works.

478 Figure 6b illustrates the inverse quality factor as a function of saturation for the  
 479 same frequencies, that is, 30 Hz (solid lines) and 2 kHz (dashed lines). We observe that  
 480 the drainage process is associated with greater levels of attenuation than the imbibition  
 481 cycle for most saturation levels. We also note that the attenuation values experience strong  
 482 changes with frequency. Interestingly, the attenuation peaks associated with the imbi-  
 483 bition process are located at higher overall water saturation values than the correspond-  
 484 ing peaks during drainage. In particular, for a frequency of 30 Hz, the drainage curve  
 485 presents a peak at  $\langle S_w \rangle = 0.992$ , while the imbibition curve presents a peak at  $\langle S_w \rangle =$   
 486  $0.996$ . For a frequency of 2 kHz, the attenuation peaks are located at  $\langle S_w \rangle = 0.96$  for  
 487 drainage and at  $\langle S_w \rangle = 0.985$  for imbibition. In this last case, the imbibition process  
 488 generates greater attenuation levels than the drainage process for saturation values above  
 489 0.98. This particular characteristic of hysteresis effects on seismic signatures, where an  
 490 imbibition process generates higher attenuation than a drainage process for sufficiently  
 491 high overall saturations, has also been observed experimentally by Yin et al. (1992) for  
 492 a partially saturated Berea sandstone. Even though there is no consensus on the low-  
 493 est measurable attenuation levels in laboratory experiments, attenuation values can be

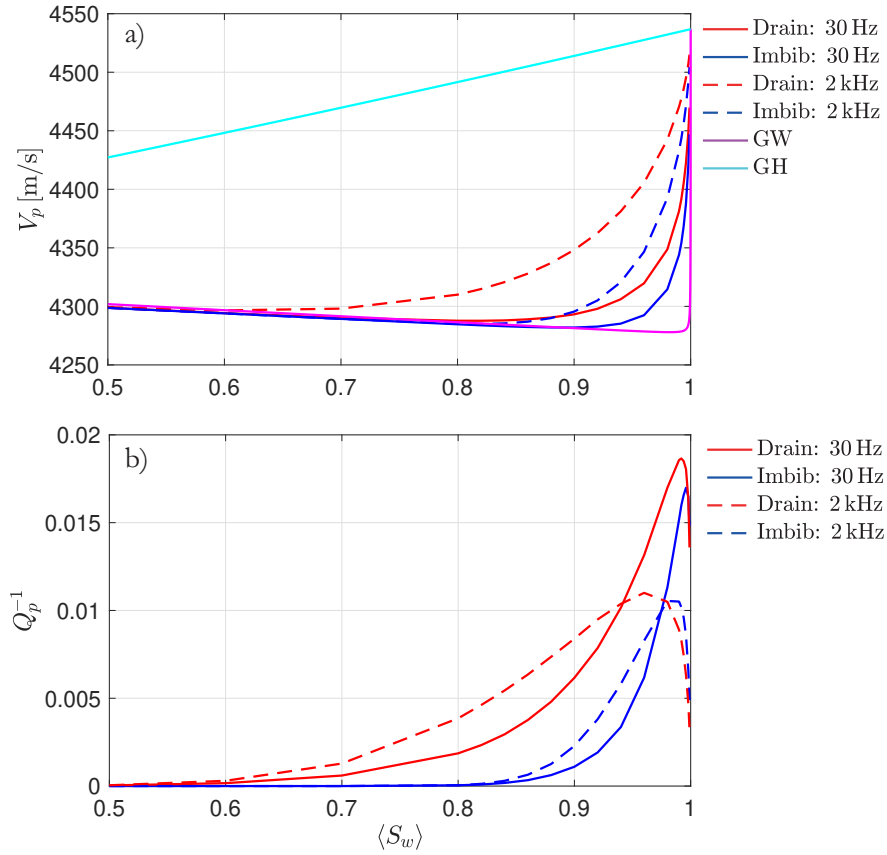


**Figure 6.** (a) Phase velocity and (b) inverse quality factor for imbibition (blue lines) and drainage (red lines) processes as functions of overall saturation. We consider two different frequencies: 30 Hz (solid lines) and 2 kHz (dashed lines). For comparison, we also show (a) the Gassmann-Wood (GW) and Gassmann-Hill (GH) models (see Appendix B).

494 measured experimentally for  $1/Q$ -values above 0.003 (Tisato & Madonna, 2012). Hence,  
 495 the attenuation levels expressed in Figure 6b are experimentally measurable for overall  
 496 water saturations above 0.84 in drainage experiments and above 0.94 in imbibition ex-  
 497 periments.

498 For a more complete analysis, we display in Figure 7 and 8 the inverse quality fac-  
 499 tor  $Q_p^{-1}$  and phase velocity  $V_p$  as functions of frequency for both drainage and imbibition  
 500 cycles. Figure 7 shows the corresponding results for both drainage (red lines) and  
 501 imbibition (blue lines) cycles as a function of frequency for overall saturation values of  
 502  $\langle S_w \rangle = 0.6$  (solid lines),  $\langle S_w \rangle = 0.7$  (circles), and  $\langle S_w \rangle = 0.8$  (dashed lines). In gen-  
 503 eral, we observe in Figures 7a and 7b that attenuation and dispersion values increase with  
 504 saturation. The reasoning for this is twofold. On the one hand, as the overall water sat-  
 505 uration of the sample increases, water patches occupy a larger portion of the medium.  
 506 It is broadly known, even in simple analytical scenarios, such as, White's model (White,  
 507 1975), that higher overall water saturation values result in stronger WIFF effects. On  
 508 the other hand, as the overall saturation of the sample increases, compressibility con-  
 509 trasts between the water patches and their surroundings increases. Consequently, the  
 510 deformation caused by a passing seismic wavefield generates stronger pressure gradients  
 511 and dissipation due to WIFF. Particularly, in Figure 7a, we note that  $Q_p^{-1}$  values asso-  
 512 ciated with the drainage cycle (red lines) present higher values than those associated with  
 513 the imbibition cycle (blue lines), which show almost negligible attenuation values. Cor-  
 514 respondingly, in Figure 7b, velocity dispersion is higher during drainage than during im-  
 515 bibition. Nevertheless, the heterogeneous saturation distributions for the overall satu-  
 516 rations illustrated in Figure 7 produce relatively low levels of seismic attenuation and  
 517 dispersion due to WIFF. Notably, attenuation levels are, at best, experimentally mea-  
 518 surable only during drainage and for  $\langle S_w \rangle = 0.8$ .

519 Figure 8 shows the seismic response for overall water saturation levels greater than  
 520 0.9. The saturation fields associated with both drainage and imbibition cycles are dis-  
 521 played in the right panels. Recall that the regions that behave effectively as water sat-  
 522 uration patches, that is, the zones where  $K_f \geq 0.5 K_w$ , are colored in white. Figures 8a  
 523 and 8b show the attenuation and phase velocity curves as a function of frequency for an  
 524 overall saturation state of  $\langle S_w \rangle = 0.9$ . Again, we observe that  $Q_p^{-1}$  and  $V_p$  values as-  
 525 sociated with the drainage cycle (red solid lines) present higher values than those asso-  
 526 ciated with the imbibition cycle (blue solid lines). Figures 8c and 8d show that for an

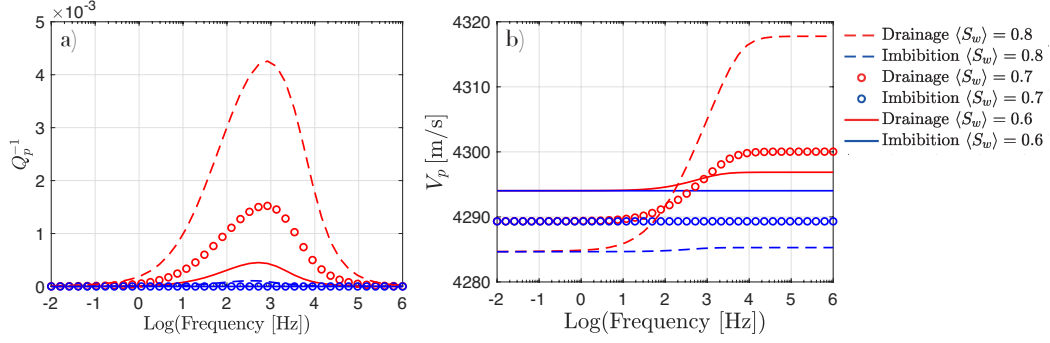


**Figure 7.** (a) Inverse quality factor and (b) phase velocity for imbibition (blue lines) and drainage (red lines) processes as functions of frequency. We consider three cases with different overall saturation values:  $\langle S_w \rangle = 0.6$  (solid lines),  $\langle S_w \rangle = 0.7$  (circles), and  $\langle S_w \rangle = 0.8$  (dashed lines).

527 overall saturation of  $\langle S_w \rangle = 0.96$ , attenuation and phase velocity values are higher than  
 528 for  $\langle S_w \rangle = 0.9$ . However, the discrepancy between the attenuation and phase velocity  
 529 curves associated with drainage and imbibition, that is, the effect of the hysteresis on  
 530 the seismic signatures, is reduced. Finally, Figures 8e and 8f show the seismic behavior  
 531 of the sample for an overall saturation of  $\langle S_w \rangle = 0.998$ . Both attenuation and phase  
 532 velocity dispersion are considerably higher than in the previous cases. We observe in Fig-  
 533 ure 8e that the hysteresis, that is, the difference between drainage and imbibition curves,  
 534 is further reduced. Hence, Figure 8 shows that the hysteresis effect on the seismic sig-  
 535 natures decreases as the porous medium reaches full saturation. In fact, the local im-  
 536 bibition and drainage capillary pressure-saturation curves approach each other in the limit  
 537 of full saturation (Figure 2). Interestingly, we observe in Figure 8e that, for frequencies  
 538 above 20 Hz, the inverse quality factor associated with imbibition is higher than the one  
 539 associated with drainage. This behavior was observed previously in Figure 6 for such sat-  
 540 uration values. This analysis shows that saturation hysteresis effects on seismic signa-  
 541 tures are highly complex and that, even if drainage processes tend to be associated with  
 542 higher levels of dissipation due to WIFF, this might not be the case when the porous medium  
 543 is close to the full saturation.

544 We have observed in Figure 8 that the frequency associated with the maximum at-  
 545 tenuation value,  $f_c$ , exhibits different values for drainage and imbibition and, also, that  
 546 these values vary with the overall saturation. This is an interesting phenomenon, the anal-

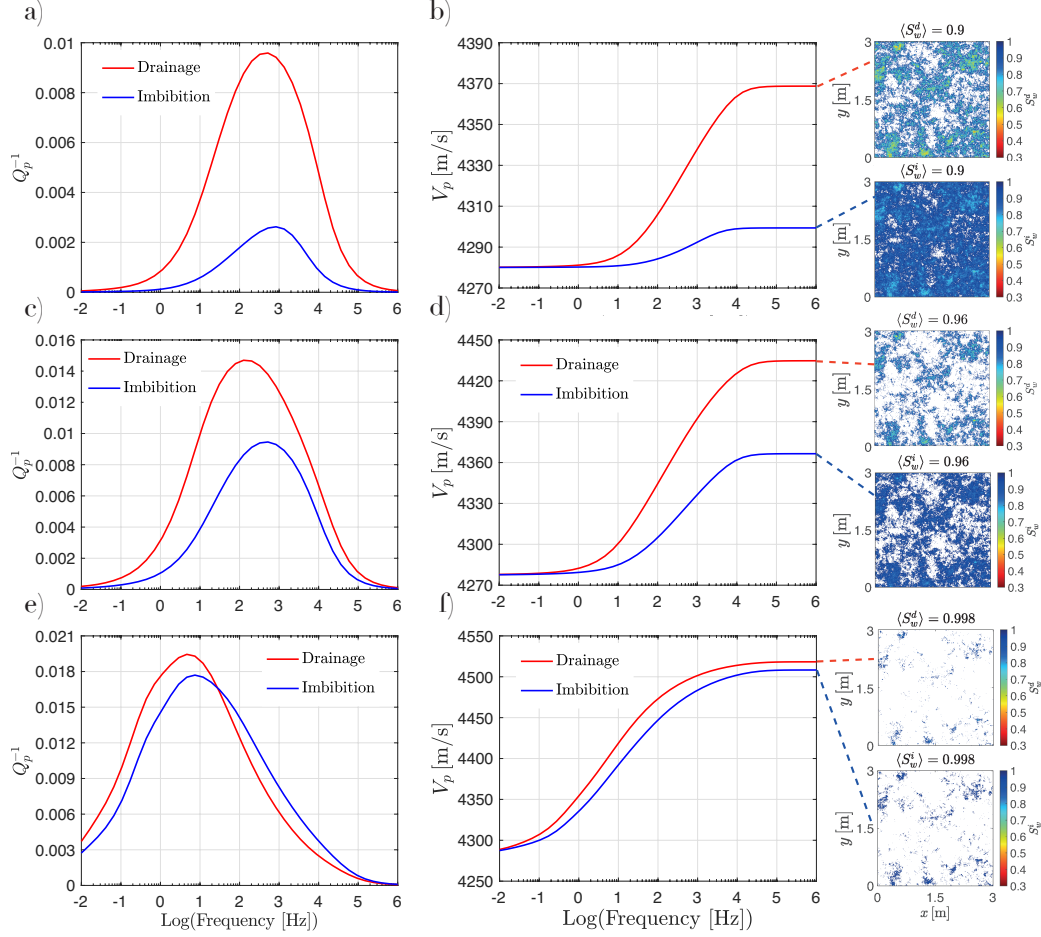


**Figure 8.** Inverse quality factor and phase velocity for imbibition (blue solid lines) and drainage (red solid lines) processes as functions of frequency. We consider three cases with different overall saturation values: (a) and (b)  $\langle S_w \rangle = 0.9$ , (c) and (d)  $\langle S_w \rangle = 0.96$ , and (e) and (f)  $\langle S_w \rangle = 0.998$ . On the right-hand side, and connected to the corresponding dispersion curves, we plot the saturation fields for both drainage and imbibition processes. White regions represent the zones where  $K_f \geq 0.5 K_w$ .

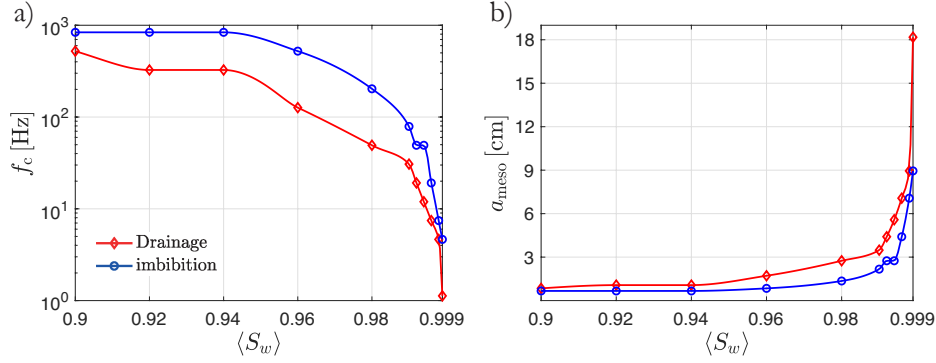


**Figure 9.** (a) Critical frequency  $f_c$  and (b) characteristic patch size  $a_{\text{meso}}$  as a function of overall saturation  $\langle S_w \rangle$ .

547 ysis of which, as further explained below, permits to estimate the characteristic size of  
 548 the water saturated patches. Figure 9a illustrates the variation of  $f_c$  with the overall sat-  
 549 uration during drainage (red line) and imbibition (blue line). The  $f_c$ -values are obtained  
 550 from the previously described attenuation curves (Figure 8). We observe that  $f_c$  decreases  
 551 with increasing overall saturation for both drainage and imbibition cycles. Also, we ob-  
 552 serve that drainage processes are associated with lower  $f_c$ -values than imbibition pro-  
 553 cesses for the same overall saturation. In order to reconcile this, it is important to re-  
 554 call that (e.g., Müller et al., 2010)

$$555 \quad f_c \simeq \frac{D}{2\pi a_{\text{meso}}^2}, \quad (17)$$

556 where  $D$  is the diffusivity of the material composing the heterogeneities where energy  
 557 dissipation occurs (equation (A8)) and  $a_{\text{meso}}$  is their characteristic size. By looking at  
 558 the panels on the right-hand side of Figure 8, it can be argued that the reduction of  $f_c$   
 559 with overall saturation is caused by an increase in the characteristic size of the water patches  
 560 with increasing water saturation. Also, patches during drainage seems to be larger than  
 561 during imbibition (Figure 8), which explains the fact that the  $f_c$ -values are higher for  
 562 the latter case.

563 Notably, equation (17) permits to estimate the characteristic size of the heterogeneities  
 564 involved in the WIFF process by using the  $f_c$ -values (Figure 9a) and an approximate value  
 565 for the diffusivity  $D$ . The latter is obtained by considering the mean porosity of the rock  
 566 in equations (14) and (15), and the fluid properties of water when computing equation  
 567 (A8). In this context, equation (17) constitutes an approximation and, as noted by Carcione



568 et al. (2003) in the context of White’s spherical patch model (White, 1975), a more rep-  
 569 resentative estimate of the characteristic water patch size is  $\sim 2a_{\text{meso}}$ , which is the dis-  
 570 tance between air patches. Figure 9b shows the behavior of  $a_{\text{meso}}$  during drainage (red  
 571 line) and imbibition (blue line) cycles. An important feature of Figure 9b is that that  
 572 the values of the characteristic patch size  $2a_{\text{meso}}$  during drainage are larger than those  
 573 associated with imbibition processes. For overall saturations varying from 0.9 to 0.999  
 574 the characteristic patch size  $2a_{\text{meso}}$  increases from 1.7 cm to 36 cm for drainage and from  
 575 1.3 cm to 18 cm for imbibition. However, by qualitatively comparing these values with  
 576 the water patches illustrated in the panels on the right-hand side of Figure 8, we note  
 577 that the latter are larger than the former. This discrepancy is expected, as in presence  
 578 of highly irregular patches, such as the ones modelled in this work, fluid pressure diffu-  
 579 sion takes place at different scales and, thus, several patch sizes can be defined. In this  
 580 sense, the  $a_{\text{meso}}$ -values derived from equation (17) are representative of the spatial scales  
 581 involved in the diffusion process for the frequency  $f_c$ .

### 582 **3.4 Effects of Throat-to-Pore Size Ratio on WIFF**

583 The radial factor  $a$ , that is, the throat-to-pore size ratio, constitutes a key pore-  
 584 scale parameter when exploring the hysteretic behavior of a porous medium. Local vari-  
 585 ations of the radial factor have an impact on the permeability and, as pore throats act  
 586 as “capillary barriers” to the flow of the non-wetting phase, on the characteristics of the  
 587 saturation field during drainage processes. The pressure relaxation process induced by  
 588 a passing P-wave is highly sensitive to changes in these properties and, hence, the effects  
 589 of the throat-to-pore size ratio on the resulting seismic signatures should be further an-  
 590 alyzed.

591 We shall explore the effects of the radial factor on WIFF considering a simple nu-  
 592 merical experiment. That is, we propose to increase all local values of the radial factor  
 593  $a(\Omega_{ij})$  by a fixed amount maintaining the original standard deviation and, thus, main-  
 594 taining the degree of spatial heterogeneity. Hence, we make the throat-to-pore size ra-  
 595 tio bigger throughout the medium. As further explained below, this experiment is per-  
 596 formed by changing the relationship between  $a$  and  $r_{max}$  displayed in Figure 3b.

597 In Figure 10a, the solid line represents the relationship between  $a$  and  $r_{max}$  con-  
 598 sidered in the previous sections, where  $a$  is characterized by a standard deviation of  $\sigma(a) =$

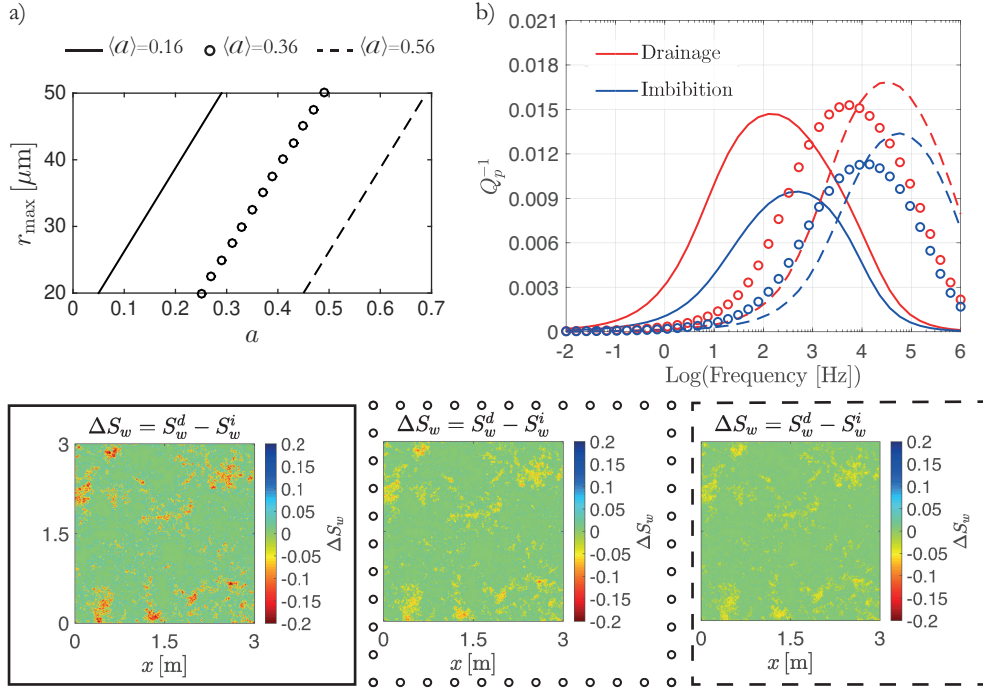


**Figure 10.** (a) Relationships between  $r_{\max}$  and  $a$  with the same standard deviation. The solid line results in a  $a$  field with  $\langle a \rangle = 0.16$ , while the circled and dashed lines correspond to  $\langle a \rangle = 0.36$  and  $\langle a \rangle = 0.56$ , respectively. (b) Inverse quality factor for imbibition (blue lines) and drainage (red lines) processes as a function of frequency for the cases considered in panel (a). At the bottom, and framed by the corresponding features (solid lines, circles, and dashed lines), we plot the difference between drainage and imbibition saturation fields for each case.

599 0.032 and a mean value of  $\langle a \rangle = 0.16$ . The circled and dashed lines represent two new  
 600 relationships characterized by the same standard deviation but with mean values of  $\langle a \rangle =$   
 601 0.36 and  $\langle a \rangle = 0.56$ , respectively. Note that, these new relationships are nothing but  
 602 an increase in the original radial factor values of 0.2 and 0.4, respectively.

603 The effects of these changes on the seismic attenuation curves are illustrated in Fig-  
 604 ure 10b, where we use red colored lines for drainage and blue lines for imbibition. The  
 605 overall saturation of the sample for this particular example is 0.96. The features employed  
 606 to represent the different relationships in Figure 10a, that is, solid lines, circles, and dashed  
 607 lines, are maintained in Figure 10b to represent the corresponding attenuation curves.  
 608 Note that the bottom panels show the difference between drainage and imbibition sat-  
 609 uration fields for each case using the same features (solid lines, circles, and dashed lines)  
 610 on the corresponding frames. On one hand in Figure 10b, we observe that, as the mean  
 611 radial factor increases, the characteristic frequency shifts to higher values. This is ex-  
 612 pected, as the permeability of the sample increases for increasing  $\langle a \rangle$  values. The incre-  
 613 ment in the local permeability values affects the diffusivity (equation (A8)) and, thus,  
 614 the characteristic frequency is shifted towards higher values (see equation (17)). On the  
 615 other hand, the increase in the porosity impacts on the effective bulk moduli of the medium,  
 616 making the rock more compliant, and, consequently, the attenuation levels rise. We also  
 617 observe that the difference between the attenuation curves associated with imbibition  
 618 and drainage cycles is reduced as the radial factor increases. It is important to recall that  
 619 the hysteretic behavior is included in the constitutive model considering constrictive seg-  
 620 ments or throats in the pore scale geometry (see Figure 1). As the radial factor increases,  
 621 the pore-scale geometry approaches that of a non-hysteretic straight-tube and, thus, hys-  
 622 teresis effects tend to disappear. This is also observed in the bottom panels, where the  
 623 differences between drainage and imbibition water saturation fields is reduced as the ra-  
 624 dial factor increases. Correspondingly, the immediate effect of increasing the radial fac-  
 625 tor is a reduction of the hysteresis effect on the saturation fields and on the seismic sig-  
 626 natures. Several phenomena, such as clogging, and precipitation/dissolution of miner-  
 627 als within the pore space have the potential to fundamentally change the characteris-  
 628 tic pore-to-throat size ratio of a porous formation. Our numerical experiments suggest  
 629 that seismic attenuation and velocity dispersion due to mesoscopic WIFF in partially  
 630 saturated media is likely to be sensible to the effects of these processes.

## 4 Conclusions

In this work, we have implemented a numerical procedure to explore saturation hysteresis effects on seismic attenuation and phase velocity dispersion due to WIFF. To do so, we generated a heterogeneous synthetic rock sample whose hydraulic properties are computed by means of a recently proposed hysteretic constitutive model. Through this approach, we obtained a set of hysteretic saturation fields representative of drainage and imbibition cycles by assuming a set of capillary equilibrium states. Considering these hysteretic fields, we then applied a numerical upscaling procedure to quantify seismic attenuation and velocity dispersion due to WIFF.

The numerical analysis shows that the hysteresis associated with drainage and imbibition processes has a significant impact on the seismic signatures. Consequently, hysteresis effects should be considered to allow for an adequate seismic characterization of partially saturated media. We also observe that phase velocities during drainage depart from the GW limit at lower overall saturation levels than during imbibition. In general, we observe that energy dissipation due to WIFF during the drainage cycle is greater than during the imbibition cycle. An analysis of the hysteretic saturation fields allowed us to demonstrate that this feature is due to the discrepancy in the spatial characteristics of the resulting saturation fields. Drainage processes tend to generate fluid patches at lower overall saturations and with more abrupt transitions towards their partially saturated surroundings than imbibition processes. This, in turn, generates more pronounced compressibility contrasts and stronger WIFF effects. Also, we observed that drainage processes tend to generate water patches with greater characteristic size than imbibition processes. Consequently, the characteristic frequency of the attenuation curve associated with drainage processes is lower than the corresponding frequency associated with imbibition. Nevertheless, as the sample approaches the limit of full saturation, hysteresis effects on WIFF tend to decrease and the discrepancy between the seismic signatures associated with drainage and imbibition processes is reduced. In this context, imbibition processes can indeed generate more attenuation than drainage processes for sufficiently high frequencies. The characteristics of the hysteretic saturation fields and of the associated seismic signatures modelled with the proposed approach were previously observed in several laboratory experiments. Hence, saturation hysteresis due to the “capillary barrier” effect constitutes a plausible explanation for the observed behavior of seis-

663 mic attenuation and the phase velocity during drainage and imbibition processes in par-  
 664 tially saturated porous media.

665 Our results also illustrate the importance of the throat-to-pore size ratio or radial  
 666 factor, as it greatly impacts the characteristics of the pore fluid distribution during drainage  
 667 and imbibition processes. In general, larger values of the radial factor generate less con-  
 668 strictive throats. This, in turn, increases the porosity and the permeability and reduces  
 669 the effects of the saturation hysteresis on the seismic signatures. Hence, seismic signa-  
 670 tures in partially saturated environments during drainage and imbibition processes are  
 671 sensitive to changes in the pore-scale characteristics of the rock frame.

## 672 **Appendix A Numerical Oscillatory Relaxation Test for Computing Seis-** 673 **mic Attenuation due to WIFF**

674 To compute the response of the sample subjected to the considered relaxation test,  
 675 we solve Biot's quasi-static poroelastic equations (Biot, 1941), which in the space-frequency  
 676 domain results in the following system of equations

$$677 \quad \nabla \cdot \boldsymbol{\tau} = 0, \quad (\text{A1})$$

$$678 \quad \nabla p_f = -i\omega \frac{\eta_f}{\kappa} \mathbf{w}, \quad (\text{A2})$$

680 where  $\boldsymbol{\tau}$  represents the total stress tensor,  $p_f$  is the pressure of the fluid, and  $\mathbf{w}$  the rel-  
 681 ative fluid-solid displacement.

682 Equations (A1) and (A2) are coupled through the stress-strain constitutive rela-  
 683 tions (Biot, 1962)

$$684 \quad \boldsymbol{\tau} = 2\mu_m \boldsymbol{\epsilon} + \mathbf{I} (\lambda_c \nabla \cdot \mathbf{u} - \alpha M \zeta), \quad (\text{A3})$$

$$685 \quad p_f = -\alpha M \nabla \cdot \mathbf{u} + M \zeta, \quad (\text{A4})$$

687 where  $\mathbf{I}$  is the identity matrix,  $\mathbf{u}$  the solid displacement, and  $\zeta = -\nabla \cdot \mathbf{w}$  a measure  
 688 of the local change in the fluid content. The strain tensor is given by  $\boldsymbol{\epsilon} = \frac{1}{2} (\nabla \mathbf{u} + (\nabla \mathbf{u})^T)$ ,  
 689 with T denoting the transpose operator. The poroelastic Biot-Willis parameter  $\alpha$ , the  
 690 fluid storage coefficient  $M$ , and the Lamé parameter  $\lambda_c$  are given by (e.g., Rubino et al.,  
 691 2009)

$$692 \quad \alpha = 1 - \frac{K_m}{K_s}, \quad (\text{A5})$$

$$693 \quad M = \left( \frac{\alpha - \phi}{K_s} + \frac{\phi}{K_f} \right)^{-1}, \quad (\text{A6})$$

695 and

$$696 \quad \lambda_c = K_m + \alpha^2 M - \frac{2}{3} \mu_m, \quad (\text{A7})$$

697 respectively. The diffusivity  $D$ , employed in equation (17), can be expressed in terms of  
 698 the poroelastic properties of the fluid saturated porous rock (e.g., Rubino & Holliger,  
 699 2012)

$$700 \quad D = \frac{\kappa}{\eta_f} \left( \frac{MH - \alpha^2 M^2}{H} \right), \quad (\text{A8})$$

701 with  $H = \lambda_c + 2\mu_m$ .

702 Equations (A1) through (A4) are numerically solved under adequate boundary con-  
 703 ditions. Let  $\Omega_{\text{sub}}$  be a square domain that represents the sample subjected to the oscil-  
 704 latory test. In addition,  $\Gamma_{\text{sub}}$  is the boundary of  $\Omega_{\text{sub}}$ . We consider the following bound-  
 705 ary conditions

$$706 \quad \mathbf{u} \cdot \boldsymbol{\nu}_{\text{sub}} = -\Delta u, \quad (x, y) \in \Gamma_{\text{sub}}^T, \quad (\text{A9})$$

$$707 \quad \mathbf{u} \cdot \boldsymbol{\nu}_{\text{sub}} = 0, \quad (x, y) \in \Gamma_{\text{sub}}^L \cup \Gamma_{\text{sub}}^R \cup \Gamma_{\text{sub}}^B, \quad (\text{A10})$$

$$708 \quad (\boldsymbol{\tau} \cdot \boldsymbol{\nu}_{\text{sub}})^T \cdot \boldsymbol{\chi}_{\text{sub}} = 0, \quad (x, y) \in \Gamma_{\text{sub}}, \quad (\text{A11})$$

$$709 \quad \mathbf{w} \cdot \boldsymbol{\nu}_{\text{sub}} = 0, \quad (x, y) \in \Gamma_{\text{sub}}, \quad (\text{A12})$$

710 where  $\Gamma_{\text{sub}}^L$ ,  $\Gamma_{\text{sub}}^R$ ,  $\Gamma_{\text{sub}}^B$ , and  $\Gamma_{\text{sub}}^T$  are the left, right, bottom, and top boundaries of the  
 711 sample, respectively, and  $\boldsymbol{\nu}_{\text{sub}}$  and  $\boldsymbol{\chi}_{\text{sub}}$  are the unit normal and the unit tangent of the  
 712 sample's boundary  $\Gamma_{\text{sub}}$ , respectively.

713 A finite-element procedure is then employed to solve equations (A1)-(A4) under  
 714 the above boundary conditions. We use bilinear functions to approximate the solid dis-  
 715 placement vector and a closed sub-space of the vector part of the Raviart-Thomas-Nedelec  
 716 space of zero order for representing the relative fluid displacement (Raviart & Thomas,  
 717 1977; Nedelec, 1980). Assuming that the volume average responses of the probed sam-  
 718 ple can be represented by an equivalent homogeneous isotropic viscoelastic solid, the re-  
 719 sulting averages over the sample's volume of the vertical components of the stress and  
 720 strain fields,  $\langle \tau_{yy}(\omega) \rangle$  and  $\langle \epsilon_{yy}(\omega) \rangle$ , allow to compute a complex-valued frequency-dependent  
 721 equivalent plane-wave modulus

$$722 \quad M_c(\omega) = \frac{\langle \tau_{yy}(\omega) \rangle}{\langle \epsilon_{yy}(\omega) \rangle}. \quad (\text{A13})$$

## Appendix B Velocity Estimates for the Relaxed and Unrelaxed States

The dependence of the phase velocity on the overall saturation is usually described employing Gassmann's model (Gassmann, 1951), which assumes that the porous medium is homogeneous and saturated by a single fluid phase. If multiple fluid phases are present in the pore space, the effective fluid bulk modulus can be estimated using Wood's and Hill's formulae (Mavko et al., 2009). These expressions allow to obtain the relaxed and unrelaxed state limits for the phase velocity, respectively. Correspondingly, if the frequency is sufficiently low such that the fluid pressure is equilibrated during a wave cycle, equation (11) can be applied to calculate an effective fluid bulk modulus of the medium  $K_f^{\text{GW}}$ . Then, the effective plane wave modulus of the rock can be obtained from the Gassmann-Wood relation

$$H^{\text{GW}} = K_m + \frac{4}{3}\mu_m + \alpha^2 M(K_f^{\text{GW}}), \quad (\text{B1})$$

where  $M(K_f^{\text{GW}})$  implies that the fluid storage coefficient is computed using the properties of the effective fluid. Conversely, the effective plane wave modulus in the high-frequency limit is given by Hill's average (e.g., Johnson, 2001)

$$H^{\text{GH}} = \frac{\langle S_w \rangle}{H^w} + \frac{(1 - \langle S_w \rangle)}{H^n}, \quad (\text{B2})$$

where  $H^q = K_m + \frac{4}{3}\mu_m + \alpha^2 M(K_q)$ , with  $q = w, n$ . Consequently, the Gassmann-Wood and Gassmann-Hill relaxed and unrelaxed phase velocity limits correspond to

$$V_p^{\text{GW}} = \sqrt{\frac{H^{\text{GW}}}{\rho_b}}, \quad \text{and} \quad V_p^{\text{GH}} = \sqrt{\frac{H^{\text{GH}}}{\rho_b}}, \quad (\text{B3})$$

respectively. Due to the fact that the sample considered in this work is not homogeneous, effective equivalent properties for these two models are required. We then compute  $K_m^{\text{eq}}$ ,  $\rho_b^{\text{eq}}$ ,  $\mu_m^{\text{eq}}$ ,  $\alpha^{\text{eq}}$ , and  $M^{\text{eq}}$  employing the mean porosity  $\langle \phi \rangle$  in the relations (14) and (15). These values are then employed in the equations (B1) and (B2).

### Acknowledgments

Part of this work was completed within the Swiss Competence Center for Energy Research-Supply of Electricity with support of Innosuisse. J. G. R. gratefully acknowledges the financial support received from the *Agencia Nacional de Promoción Científica y Tecnológica* of Argentina (PICT 2017-2976). The authors thank Eva Caspari for enlightening discussions and two anonymous reviewers for lucid comments and insightful suggestions. The hysteretic saturation fields and the seismic attenuation and velocity dispersion data for this paper are available from <https://github.com/PoroelasticityUNIL/Hysteresis>.

754 **References**

- 755 Akbar, N., Mavko, G., Nur, A., & Dvorkin, J. (1994). Seismic signatures of reser-  
 756 voir transport properties and pore fluid distribution. *Geophysics*, *59*(8), 1222–  
 757 1236.
- 758 Alemu, B. L., Aker, E., Soldal, M., Johnsen, Ø., & Aagaard, P. (2013). Effect  
 759 of sub-core scale heterogeneities on acoustic and electrical properties of a  
 760 reservoir rock: A CO<sub>2</sub> flooding experiment of brine saturated sandstone in a  
 761 computed tomography scanner. *Geophys. Prospect.*, *61*, 235-250.
- 762 Ba, J., Carcione, J. M., & Sun, W. (2015). Seismic attenuation due to hetero-  
 763 geneities of rock fabric and fluid distribution. *Geophys. J. Int.*, *202*(3), 1843–  
 764 1847.
- 765 Bear, J. (1972). *Dynamics of Fluids in Porous Media*. New York: Am. Elsevier.
- 766 Biot, M. A. (1941). General theory of three-dimensional consolidation. *J. Appl.*  
 767 *Phys.*, *12*, 155-164. doi: 10.1063/1.1712886
- 768 Biot, M. A. (1962). Mechanics of deformation and acoustic propagation in porous  
 769 media. *J. Appl. Phys.*, *33*(4), 1482-1498. doi: 10.1063/1.1728759
- 770 Borchardt, R. D. (2009). *Viscoelastic Waves in Layered Media*. Cambridge Univer-  
 771 sity Press.
- 772 Bourbié, T., & Zinszner, B. (1985). Hydraulic and acoustic properties as a function  
 773 of porosity in Fontainebleau sandstone. *J. Geophys. Res.*, *90*, 11524–11532.
- 774 Brooks, R., & Corey, A. (1964). *Hydraulic Properties of Porous Media*. Colorado  
 775 State University.
- 776 Cadoret, T., Marion, D., & Zinszner, B. (1995). Influence of frequency and fluid  
 777 distribution on elastic wave velocities in partially saturated limestones. *J. Geo-*  
 778 *phys. Res.*, *100*(B6), 9789–9803.
- 779 Cadoret, T., Mavko, G., & Zinszner, B. (1998). Fluid distribution effect on sonic at-  
 780 tenuation in partially saturated limestones. *Geophysics*, *63*, 154–160.
- 781 Carcione, J. M., Helle, H. B., & Pham, N. H. (2003). White’s model for wave prop-  
 782 agation in partially saturated rocks: Comparison with poroelastic numerical  
 783 experiments. *Geophysics*, *68*(4), 1389–1398.
- 784 Chapman, S., Tisato, N., Quintal, B., & Holliger, K. (2016). Seismic attenuation  
 785 in partially saturated Berea sandstone submitted to a range of confining pres-  
 786 sures. *J. Geophys. Res.*, *121*(3), 1664-1676.



- 787 Dong, H., & Blunt, M. J. (2009). Pore-network extraction from micro-computerized-  
788 tomography images. *Phys. Rev. E*, *80*(3), 036307.
- 789 Doyen, P. M. (1988). Permeability, conductivity, and pore geometry of sandstone. *J.*  
790 *Geophys. Res. Solid Earth*, *93*(B7), 7729–7740.
- 791 Gassmann, F. (1951). Über die Elastizität poröser Medien. *Vierteljahresschr. Natur-*  
792 *forsch. Ges. Zürich*, *96*, 1–23.
- 793 Guarracino, L. (2007). Estimation of saturated hydraulic conductivity  $k_s$  from the  
794 van genuchten shape parameter  $\alpha$ . *Water Resour. Res.*, *43*(11).
- 795 Guarracino, L., Rötting, T., & Carrera, J. (2014). A fractal model to describe the  
796 evolution of multiphase flow properties during mineral dissolution. *Adv. Water*  
797 *Resour.*, *67*, 78–86.
- 798 Hogarth, W. L., Hopmans, J., Parlange, J. Y., & Haverkamp, R. (1988). Application  
799 of a simple soil-water hysteresis model. *J. Hydrol.*, *98*(1-2), 21–29.
- 800 Johnson, D. L. (2001). Theory of frequency dependent acoustics in patchy-saturated  
801 porous media. *J. Acoust. Soc. Am.*, *110*, 682-694. doi: 10.1121/1.1381021
- 802 Juanes, R., Spiteri, E. J., Orr, F. M., & Blunt, M. J. (2006). Impact of relative per-  
803 meability hysteresis on geological CO<sub>2</sub> storage. *Water Resour. Res.*, *42*(12).
- 804 Kearey, P., Brooks, M., & Hill, I. (2013). *An Introduction to Geophysical Explo-*  
805 *ration*. John Wiley & Sons.
- 806 Knight, R., & Nolen-Hoeksema, R. (1990). A laboratory study of the dependence  
807 of elastic wave velocities on pore scale fluid distribution. *Geophys. Res. Lett.*,  
808 *17*(10), 1529–1532.
- 809 Krause, M., Krevor, S., & Benson, S. M. (2013). A procedure for the accurate deter-  
810 mination of sub-core scale permeability distributions with error quantification.  
811 *Transport Porous Med.*, *98*(3), 565–588.
- 812 Krevor, S., Pini, R., Li, B., & Benson, S. M. (2011). Capillary heterogeneity trap-  
813 ping of CO<sub>2</sub> in a sandstone rock at reservoir conditions. *Geophys Res. Lett.*,  
814 *38*(15).
- 815 Lebedev, M., Toms-Stewart, J., Clennell, B., Peruvukhina, M., Shulakova, V., Pa-  
816 terson, L., . . . Wenzlau, F. (2009). Direct laboratory observation of patchy  
817 saturation and its effects on ultrasonic velocities. *The Leading Edge*, *28*(1),  
818 24-27.
- 819 Lenhard, R. J., Parker, J. C., & Kaluarachchi, J. J. (1991). Comparing simulated

- 820 and experimental hysteretic two-phase transient fluid flow phenomena. *Water*  
821 *Resour. Res.*, *27*(8), 2113–2124.
- 822 Lenormand, R. (1990). Liquids in porous media. *J. Phys. Condens. Matter*, *2*, 79–  
823 88.
- 824 Lenormand, R., Zarcone, C., & Sarr, A. (1983). Mechanisms of the displacement of  
825 one fluid by another in a network of capillary ducts. *J. Fluid Mech.*, *135*, 337–  
826 353.
- 827 Le Ravalec, M., Guéguen, Y., & Chelidze, T. (1996). Elastic wave velocities in par-  
828 tially saturated rocks: Saturation hysteresis. *J. Geophys. Res.*, *101*, 837–844.
- 829 Li, B., & Benson, S. M. (2015). Influence of small-scale heterogeneity on upward  
830 CO<sub>2</sub> plume migration in storage aquifers. *Adv. Water Resour.*, *83*, 389–404.
- 831 Masson, Y. J., & Pride, S. R. (2011). Seismic attenuation due to patchy saturation.  
832 *J. Geophys. Res.*, *116*, B0326. doi: 10.1029/2010JB007983
- 833 Mavko, G., Mukerji, T., & Dvorkin, J. (2009). *The Rock Physics Handbook: Tools*  
834 *for Seismic Analysis of Porous Media*. Cambridge University Press.
- 835 Monsen, K., & Johnstad, S. E. (2005). Improved understanding of velocity-  
836 saturation relationships using 4D computer-tomography acoustic measure-  
837 ments. *Geophys. Prospect.*, *53*(2), 173–181.
- 838 Müller, T. M., Gurevich, B., & Lebedev, M. (2010). Seismic wave attenuation and  
839 dispersion resulting from wave-induced flow in porous rocks - a review. *Geo-*  
840 *physics*, *75*, 147-163. doi: 10.1190/1.3463417
- 841 Nakagawa, S., Kneafsey, T. J., Daley, T. M., Freifeld, B. M., & Rees, E. V. (2013).  
842 Laboratory seismic monitoring of supercritical CO<sub>2</sub> flooding in sandstone  
843 cores using the split hopkinson resonant bar technique with concurrent X-ray  
844 computed tomography imaging. *Geophys. Prospect.*, *61*(2), 254-269.
- 845 Nedelec, J. C. (1980). Mixed finite elements in  $r^3$ . *Numer. Math.*, *35*, 315-341. doi:  
846 10.1007/BF01396415
- 847 Papageorgiou, G., & Chapman, M. (2015). Multifluid squirt flow and hysteresis  
848 effects on the bulk modulus–water saturation relationship. *Geophys. J. Int.*,  
849 *203*(2), 814–817.
- 850 Perrin, J.-C., & Benson, S. (2010). An experimental study on the influence of sub-  
851 core scale heterogeneities on CO<sub>2</sub> distribution in reservoir rocks. *Transport*  
852 *Porous Med.*, *82*(1), 93–109.

- 853 Pini, R., Krevor, S. C., & Benson, S. M. (2012). Capillary pressure and heterogene-  
 854 ity for the CO<sub>2</sub>/water system in sandstone rocks at reservoir conditions. *Adv.*  
 855 *Water Resour.*, *38*, 48–59.
- 856 Pride, S. R. (2005). Relationships between seismic and hydrological properties. In  
 857 Y. Rubin & S. Hubbard (Eds.), *Hydrogeophysics* (pp. 253–290). Springer.
- 858 Raviart, P., & Thomas, J. (1977). Mixed finite element method for 2nd order elliptic  
 859 problems. *Lect. Notes Math.*, *606*, 292–315. doi: 10.1007/BFb0064470
- 860 Rubino, J. G., & Holliger, K. (2012). Seismic attenuation and velocity dispersion  
 861 in heterogeneous partially saturated porous rocks. *Geophys. J. Int.*, *188*, 1088–  
 862 1102. doi: 10.1111/j.1365-246X.2011.05291.x
- 863 Rubino, J. G., & Holliger, K. (2013). Research note: Seismic attenuation due  
 864 to wave-induced fluid flow at microscopic and mesoscopic scales. *Geophys.*  
 865 *Prospect.*, 882–889. doi: 10.1111/1365-2478.12009
- 866 Rubino, J. G., Ravazzoli, C. L., & Santos, J. E. (2009). Equivalent viscoelastic solids  
 867 for heterogeneous fluid-saturated porous rocks. *Geophysics*, *74*, N1–N13. doi:  
 868 10.1190/1.3008544
- 869 Rubino, J. G., Velis, D. R., & Sacchi, M. D. (2011). Numerical analysis of wave-  
 870 induced fluid flow effects on seismic data: Application to monitoring of  
 871 CO<sub>2</sub> storage at the Sleipner field. *J. Geophys. Res.*, *116*, 1088–1102. doi:  
 872 10.1029/2010JB007997
- 873 Shi, J., Xuw, Z., & Durucan, S. (2011). Supercritical CO<sub>2</sub> core flooding and im-  
 874 bibition in Tako sandstone- Influence of sub-core scale heterogeneity. *Int. J.*  
 875 *Greenh. Gas Con.*, *5*, 75–87. doi: 10.1016/j.ijggc.2010.07.003
- 876 Solazzi, S. G. (2018). *Modelado y análisis de la respuesta sísmica de rocas het-*  
 877 *erogéneas saturadas por fluidos inmiscibles* (PhD thesis, Facultad de Ciencias  
 878 Astronómicas y Geofísicas, Universidad Nacional de La Plata). Retrieved from  
 879 SEDICI. (<http://sedici.unlp.edu.ar/handle/10915/67336>).
- 880 Soldi, M., Guarracino, L., & Jougnot, D. (2017). A simple hysteretic constitutive  
 881 model for unsaturated flow. *Transport Porous Med.*, *120*(2), 271–285.
- 882 Subramaniyan, S., Quintal, B., Madonna, C., & Saenger, E. H. (2015). Laboratory-  
 883 based seismic attenuation in fontainebleau sandstone: Evidence of squirt flow.  
 884 *J. Geophys. Res. Solid Earth*, *120*(11), 7526–7535.
- 885 Teja, A. S., & Rice, P. (1981). Generalized corresponding states method for viscosi-

- 886 ties of liquid mixtures. *Ind. Eng. Chem. Fundam.*, *20*, 77–81.
- 887 Timur, A. (1968). An investigation of permeability, porosity, and residual water sat-  
888 uration relationships. In *SPWLA 9th Annual Logging Symposium*.
- 889 Tisato, N., & Madonna, C. (2012). Attenuation at low seismic frequencies in par-  
890 ially saturated rocks: Measurements and description of a new apparatus. *J.*  
891 *Appl. Geophys.*, *86*, 44 – 53.
- 892 Tisato, N., & Quintal, B. (2013). Measurements of seismic attenuation and transient  
893 fluid pressure in partially saturated Berea sandstone: Evidence of fluid flow on  
894 the mesoscopic scale. *Geophys. J. Int.*, *195*, 342–351. doi: 10.1093/gji/ggt259
- 895 Toms-Stewart, J., Müller, T. M., Gurevich, B., & Paterson, L. (2009). Statistical  
896 characterization of gas-patch distributions in partially saturated rocks. *Geo-*  
897 *physics*, *72(2)*, WA51–WA64.
- 898 Tronicke, J., & Holliger, K. (2005). Quantitative integration of hydrogeophysical  
899 data: Conditional geostatistical simulation for characterizing heterogeneous  
900 alluvial aquifers. *Geophysics*, *70*, H1–H10. doi: 10.1190/1.1925744
- 901 Tyler, S. W., & Wheatcraft, S. W. (1990). Fractal processes in soil water retention.  
902 *Water Resour. Res.*, *26(5)*, 1047–1054.
- 903 van Genuchten, M. T. (1980). A closed-form equation for predicting the hydraulic  
904 conductivity fo unsaturated soils. *Soil Sci. Soc. Am. J.*, *44*, 892–898.
- 905 Vargaftik, N. B., Volkov, B. N., & Voljak, L. D. (1983). International tables of the  
906 surface tension of water. *J. Phys. Chem. Ref. Data*, *12(3)*, 817–820.
- 907 White, J. E. (1975). Computed seismic speeds and attenuation in rocks with partial  
908 gas saturation. *Geophysics*, *40*, 224–232. doi: 10.1190/1.1440520
- 909 Wood, A. (1955). *A Textbook of Sound*. New York: MacMillan Publishing Com-  
910 pany.
- 911 Xu, P. (2015). A discussion on fractal models for transport physics of porous media.  
912 *Fractals*, *23(03)*, 1530001.
- 913 Yin, C. S., Batzle, M. L., & Smith, B. J. (1992). Effects of partial liquid/gas satura-  
914 tion on extensional wave attenuation in Berea sandstone. *Geophys. Res. Lett.*,  
915 *19(13)*, 1399–1402.
- 916 Yu, B., Li, J., Li, Z., & Zou, M. (2003). Permeabilities of unsaturated fractal porous  
917 media. *Int. J. Multiph. Flow*, *29(10)*, 1625–1642.
- 918 Zhang, Y., Nishizawa, O., Kiyama, T., & Xue, Z. (2015). Saturation-path de-

919 pendency of P-wave velocity and attenuation in sandstone saturated with  
920 CO<sub>2</sub> and brine revealed by simultaneous measurements of waveforms and  
921 X-ray computed tomography images. *Geophysics*, 80, D403–D415. doi:  
922 10.1190/GEO2014-0289.1